Middle to late Pleistocene stability of the central East Antarctic Ice Sheet at the head of Law Glacier

M.R. Kaplan[1], K. Licht[2], G. Winckler[1,3], J.M. Schaefer[1,3], N. Bader[2], C. Mathieson[1], M. Roberts[4], C.M. Kassab[2], R. Schwartz[1], and J. A. Graly[2]

[1]Division of Geochemistry, Lamont-Doherty Earth Observatory, Palisades, NY 10964, USA
[2]Department of Earth Sciences, IUPUI, Indianapolis, IN 46202
[3]Department of Earth and Environmental Sciences, Columbia University, New York, NY 10027, USA

[4]2 Finch Street, Albert Town, Wanaka, New Zealand

This PDF file includes Materials and Methods, Figs. DR1 to DR5, and Tables DR1 to DR4

Sediment and moraine formation in the Mt. Achernar blue ice region

The first key point is that blue ice moraines are associated with blue ice areas, where sublimation dominates mass balance, as discussed in the main text (Whillans and Cassidy, 1983; Chinn, 1991, 1994; Cassidy et al., 1992; Sinisalo and Moore, 2010; Fogwill et al., 2011; Campbell et al., 2014; Hein et al., 2016). In Figures 1C and DR1A, the conceptual model of how such moraines form is based on extensive descriptions and concepts in these prior publications, and observations locally at Mt. Achernar (Scarrow et al., 2013; Bader et al., 2017). At this site, observations indicate that sediment entrained in and transported by the underlying ice is exposed at the surface over time via sublimation. On average 20% of pebbles on the moraine surface are faceted and/or striated suggesting a mix of basal and englacial transport (Bader et al., 2017).

The second key point is that the surface sediments overlie ice. The age progression implies that debris accretes laterally over time, which is consistent with the provenance-based interpretation of Bader et al. (2017). The debris also thickens with time (Scarrow et al., 2013; Bader et al., 2017). Yet, in comparison to moraines directly overlying bedrock − as is typically the case for "non-blue ice moraines" – the sediment-moraine shown in Figures 1 to 3 overlies ice that remains contiguous with the active Law outlet glacier. Bader et al. (2017) inferred the innermost 1-2 km of sediment-moraine (clean) is still most actively connected to the Law Glacier and connecting debris.

Thus, at Mt. Achernar, major changes in the elevation of the Law (and contiguous EAIS) glacier surface would be expected to alter markedly the flow in the ice underlying the sediment-moraines. For example, increases in ice elevation (thickening of Law Glacier) eventually may deform the moraine bands as observed in other areas (Chinn, 1991, 1994). For comparison, large decreases in ice elevation (thinning of Law Glacier) would result in reversal of flow and carry the surficial moraine out of the area.

At Mt. Achernar, not only are the bands quasi-continuous, mimicking the present moraine-active ice boundary, but there are bands of discrete petrologic compositions for several kilometres in places (Bader et al., 2017); these are visible in Figures 2 and DR3. Thus, we infer that the relatively undeformed nature of the moraine bands (including compositional bands) at Mt. Achernar reflects a long-lasting stability of ice flow from the respective ice sources.

Bader et al. (2017) also discussed in detail other changes in moraine morphology and sediment provenance (Fig. DR1A). For example, they documented that relatively minor changes indeed occurred in ice behaviour (<40 m surface elevation), as shown in Figure 3 and discussed in main text of this paper. However, such changes were not enough to deform or drain the blue ice moraine at Mt. Achernar (Chinn, 1991, 1994). Based on the evidence, Bader et al. (2017) concluded the Law Glacier has tapped into and eroded successively lower stratigraphic units of the Beacon Supergroup (Fig. DR1A).

Last, on sunny days, minor amount of supraglacial melting was observed. The melting appears to be associated with the dark debris, especially near the boundary between the moraine and clean Law Glacier (Fig. DR2E). Also, a minor amount of melting was observed in the youngest (10^3 time scale) zone during the 2016/2017 austral summer. The relationship between melting and boulder/clast history, if any, is not yet clear.

Cosmogenic nuclide data

In austral summer 2010/2011, we collected quartz bearing sandstones and pyroxene bearing dolerites that appeared relatively stable (Figs. DR1, DR2). For example, we preferentially selected boulders away from hummocks. If necessary, we sampled the top of a hummock. We also preferred large table-shaped rectangular boulders (Fig. DR2); the idea is that although such boulders may have shifted somewhat, they are less likely to have completely flipped over, exposing a new side. Shifting of boulders could lead to ages being minima for when they arrived at the surface.

Samples were collected close to the topographic profile shown in Figure 2 (or DR4), which was the focus of provenance study in Bader et al. (2017). All samples were collected within ~500 m of the profile. The profile was taken with a rover GPS backpacking system. We note that samples MAR-11-23 and -30 are indeed on two different ridges, separated by a depression, as shown on Figure 3 (DR4), although they may appear to be on the same ridge given the scale of Figure 2B.

Samples were taken from the upper 1-3 cm from the most stable-looking flattish section, and if possible the center, of the boulder's top surface. Samples were collected with hammer and chisel. The azimuthal elevations of the surrounding landscape were measured using a compass and clinometer. We used a Trimble GPS system relative to the WGS 1984 datum to measure position including altitudes. All measurements were corrected differentially using continuous data from a base station set up at a semi-permanent camp for the field season. Post-processed uncertainties (1σ) are <1 m for latitude-longitude and altitudes.

Regarding geologic effects on ages, first all ages assume no erosion. As Antarctica has some of the lowest erosion rates on Earth, this is negligible on the time scale discussed here. Some of the boulders are still striated (e.g., MAR-11-18, ~ 6-5 ka). Nonetheless, we point out that if we assume an erosion rate of ~10 cm Ma^{-1}, the 5 ka and 550 ka ages (youngest and oldest) increase by <5 years and ~5%, respectively; an erosion rate of 20 cm Ma^{-1} causes an increase of by <5 years (0.08%) and ~10%, respectively. Also, we do not correct for snow cover on the boulders. We point out that this environment is one of the driest on Earth, and by definition blue ice areas contain generally little or no snow (Bintanja, 1999). Although some snow may accumulate in small depressions, we avoided such spots. On the other hand, Hagen (1995) noted 1 young outlier of ~15 ka could be explained by the fact it was collected from a depression with snow (Fig. 2A).

^{10}Be, ^{26}Al

Details of processing and age calculations are provided in Tables DR1 and DR2 and shown on Figures 2 and 3, DR3, and DR4. Samples were processed using standard methods (Schaefer et al., 2009) and measured at the Center for Accelerator Mass Spectrometry at Lawrence Livermore National Laboratory (CAMS-LLNL). For age calculations, we used the production rate published in (Kaplan et al., 2011), which is the closest to Antarctica, at ~50°S. This rate is statistically indistinguishable from the other Southern Hemisphere production rate, derived in New Zealand at ~43°S (Putnam et al., 2010).

^{3}He

Processing of pyroxene separates followed the procedure outlined in Bromley et al. (2014) and Eaves et al. (2015, 2016). Abundance and isotopic analyses are performed with a MAP215-50 noble gas mass spectrometer (e.g., calibrated with a known volume of a Yellowstone helium standard (MM)). Details of measurements are provided in Table DR4.

For simplicity, all ages presented in the main text do not account for noncosmogenic ^{3}He in the samples. That is, the ages are presented with the assumption all ^{3}He is cosmogenically produced. However, noncosmogenic helium components (nucleogenic and inherited [mantle-derived]) may contribute a statistically significant contribution to the youngest samples in the study area (see next paragraph).

We emphasize, though, that the assumption of no nucleogenic or inherited helium has no effect on our conclusions. The reasons include: (i) critically, the findings also rely on ^{10}Be-^{26}Al ages (Figs. 2, 3). All three nuclides are in agreement that moraines steadily get older; (ii) any potential correction becomes smaller as the ^{3}He age increases. By 100 ka, the noncosmogenic ^{3}He component is at least an order of magnitude less than total ^{3}He concentration: this estimate is based on the following. The two Ferrar dolerite samples that afford the youngest age (both ~6.7 ka), also can be used to estimate the upper limit for the concentration of noncosmogenic ^{3}He (Fig. 2). If we subtract the (statistically identical) average ^{3}He concentration of these two samples from the concentrations in all other Helium samples, it reduces their respective ages. These adjusted ages are shown in Figures DR3 and DR4, which are identical to Figures 2 and 3 in main text, except they assume there is a maximum of ~6700 years' worth of noncosmogenic ^{3}He. This equates to a maximum of about ~5 x 10^{6} atoms/g at the latitude and elevation of the Mt. Archernar samples. A concentration on the order of ~5 x 10^{6} is consistent with other estimates for the noncosmogenic ^{3}He component in the Ferrar Dolerite (e.g., Margerison et al, 2005). Moreover, we note that this correction for noncosmogenic helium overall brings the ^{10}Be-^{26}Al ages and ^{3}He ages in closer agreement for the youngest dates.

Other systematic uncertainties

For ^{10}Be-^{26}Al-^{3}He age calculations we used the methods incorporated in the CRONUS-Earth online exposure age calculator version 2.2, with version 2.2.1 of the constants file (Balco et al., 2008; with a ^{10}Be half-life of 1.39 Ma, [Nishiizumi et al., 2007]). Taken at face value, uncertainties for the production rate are ~3% and ~8% for ^{10}Be-^{26}Al and ^{3}He, respectively (Putnam et al., 2010; Kaplan et al., 2011).

At present, there are different scaling schemes available for position and elevation (Table DR2). We elected to use Lal (1991)/Stone (2000) scaling scheme, but note that the choice of has no effect on our findings. ^{3}He and ^{10}Be/^{26}Al ages will both change systematically if a different

production rate (Putnam et al., 2010; Kaplan et al., 2011) and scaling scheme are used (e.g., on Figs. 2, DR3).

With regards to the long term, for example, 10^5 year-time scale or oldest ages on Figure 2, we do not know if the production rate has changed significantly. However, we emphasize the following. First, long-term changes are likely to be reduced at 85°S, because one of the most important effects on *in situ* production is a change in the geomagnetic field. Changes in the field strength are most important at the lowest latitudes. Whereas, Mt. Achernar is close to the south geographic and geomagnetic pole. Second, such production rate changes would not affect our main conclusions.

Prior cosmogenic ages in Hagen (1995)

In one of the earliest cosmogenic dating studies in Antarctica, Hagen (1995) obtained a ^{10}Be and ^{26}Al dataset (Fig. 2). All the data in Hagen (1995) were recalculated (Table DR3) based on the up-to-date cosmogenic nuclide systematics discussed above. Similar to the new data (Tables DR1 to DR2), all of the previously obtained ^{26}Al/^{10}Be concentration ratios overlap with the constant exposure line (Fig. DR5). This result also supports our conclusion these subglacially-derived samples do not contain a complex exposure/burial history.

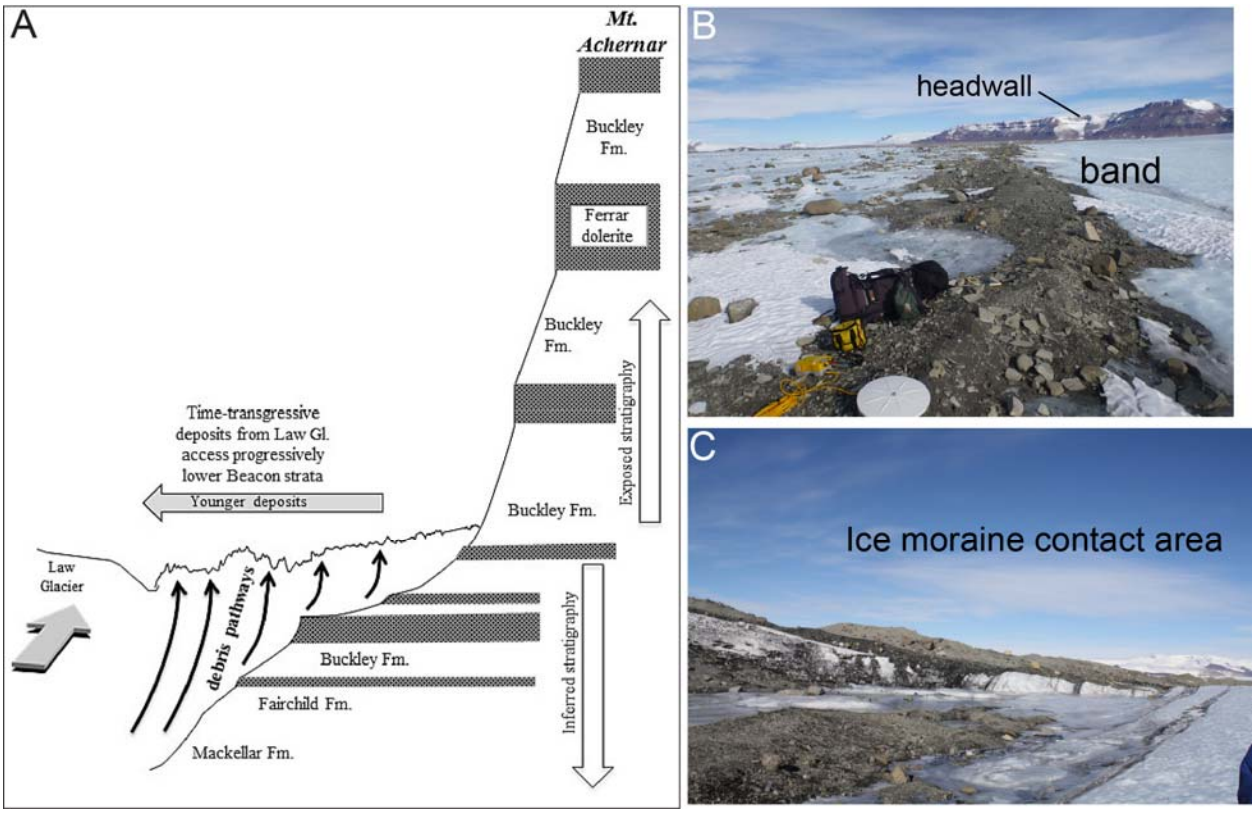

Figure DR1. A: From Bader et al. (2017). A conceptual model of blue ice moraine formation specifically at Mt. Achernar (cf., a more general model is in Figure 1C). The inferences in Figures 1C and DR1A are based on extensive descriptions in prior publications (Whillans and Cassidy, 1983; Cassidy et al., 1992; Fogwill et al., 2011; Chinn, 1991, 1994; Campbell et al., 2014; Hein et al., 2016; Bader et al. 2017). This figure shows the exposed 800 m thick bedrock (Faure and Mensing, 2010) and inferred (ice-covered) bedrock stratigraphy. Dark horizontal bands represent Ferrar dolerite sills, three of which are exposed. Black arrows show hypothesized debris transport pathways that explain the source of compositional changes in till across the moraine. This model highlights the sub- and englacial origin of the moraine sediment and spatio-temporal shift to debris sources lower in the bedrock stratigraphic section as new till accumulated toward what is the present-day Law Glacier margin. **B:** A photograph of the emerging debris band in the lower right of Figure 1B. Note that the substantial distance to the headwall (Mt. Achernar) indicates there is no local source of rockfall and the debris building up on the ice surface must be englacially or subglacially derived (cf., Fig. A). **C)** A photograph of a recently emerging band next to the ice-moraine boundary.

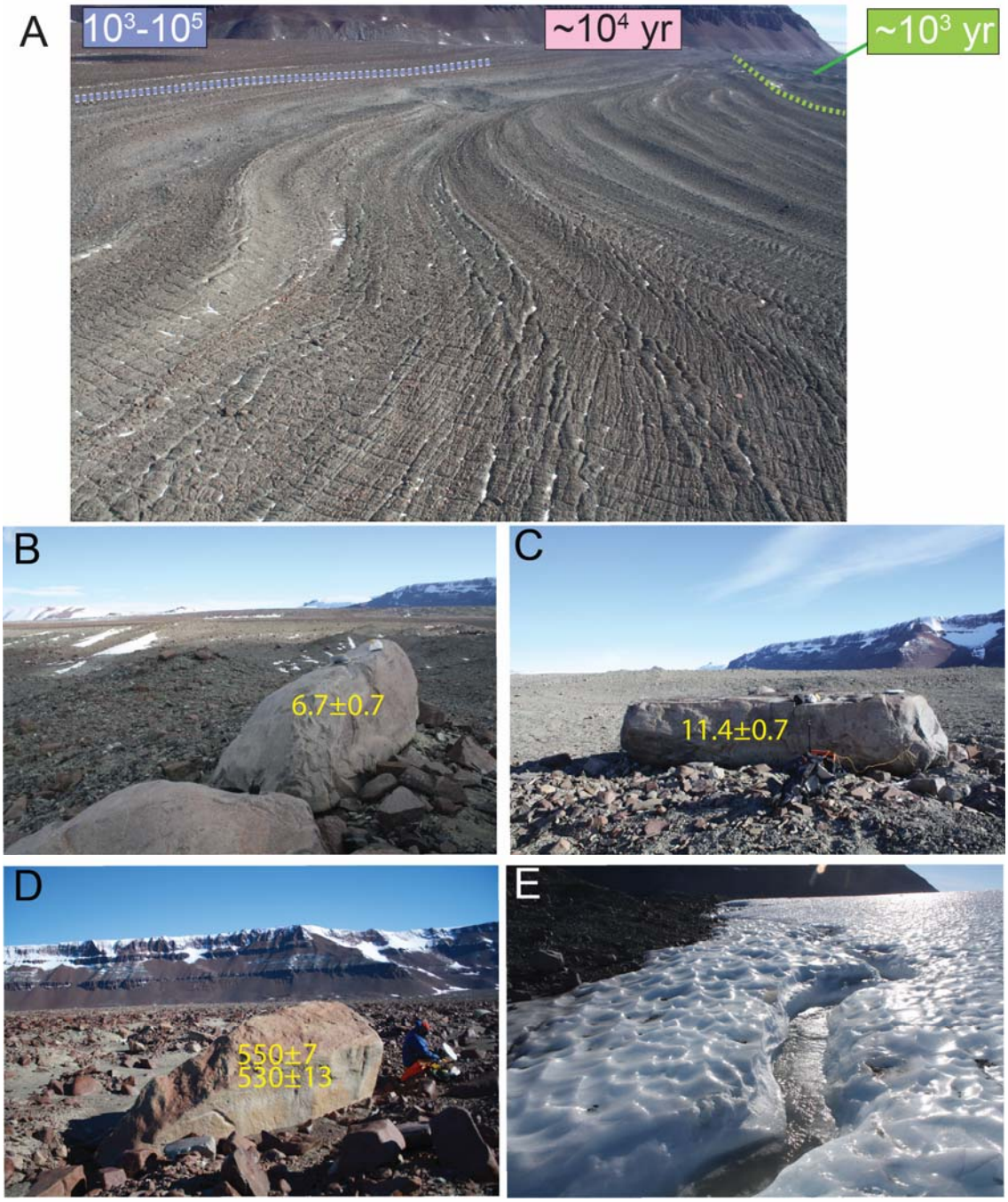

Figure DR2. A: Photo of the moraine, including ridges and depressions, at Mt. Achernar, with ages based on those shown in Figure 2. Note the increase in oxidation in the upper left. **B-D:** Photos of boulders with the youngest (B-C) and oldest (D) exposure ages. We tried to sample preferentially boulders with a flat table shape, if possible, given it may be more difficult for them to completely turn over (e.g., **C**). Note the oldest boulder (**D)** has the "most oxidized" top and it is surrounded by strongly oxidized material. In contrast, the younger samples shown in **B and C,** and their surroundings, lack the red oxidation of the older deposit. **E:** A photo that shows running water on the ice surface, January, 2011, indicating a minor amount of melting occurs in the summer close to where darker debris exists.

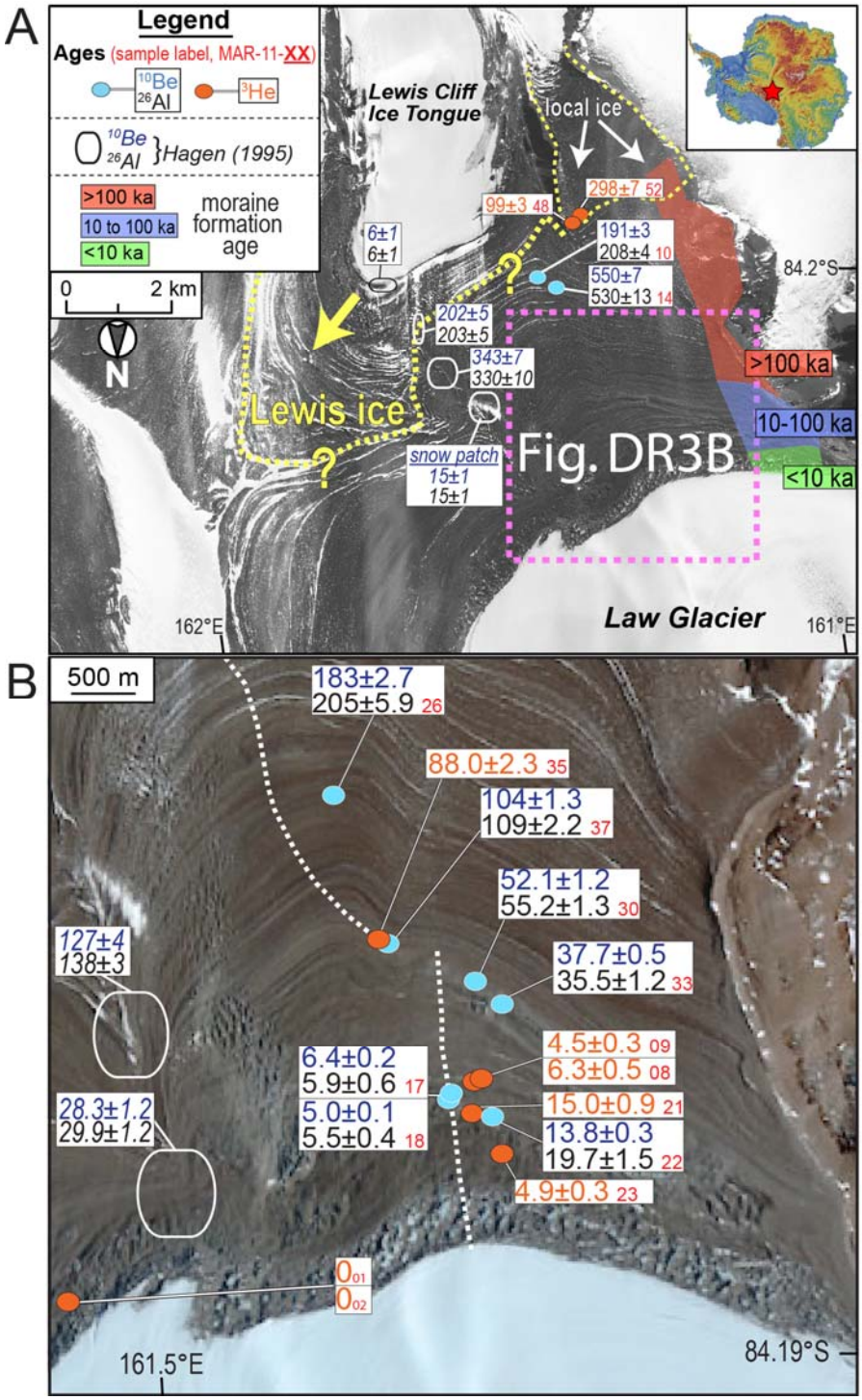

Figure DR3. Same as Figure 2, except assuming that each ^{3}He measurement contains a maximum of 5.05 x 10^{6} atoms/g of noncosmogenic ^{3}He (e.g., nucleogenic, magmatic), i.e., <6.7 ka equivalent age. This value is from the two youngest statistically identical samples, MAR-11-01 and 02, shown here in the lowermost left of panel B, and Figure 2B, and presented in Table DR4. This concentration was then subtracted from each sample's concentration, and the ages recalculated. The boundary between Law and Lewis ice is marked in yellow, which is uncertain in places (question mark). Dashed line in panel B represents profile in Figure DR4 (from Bader et al, 2017).

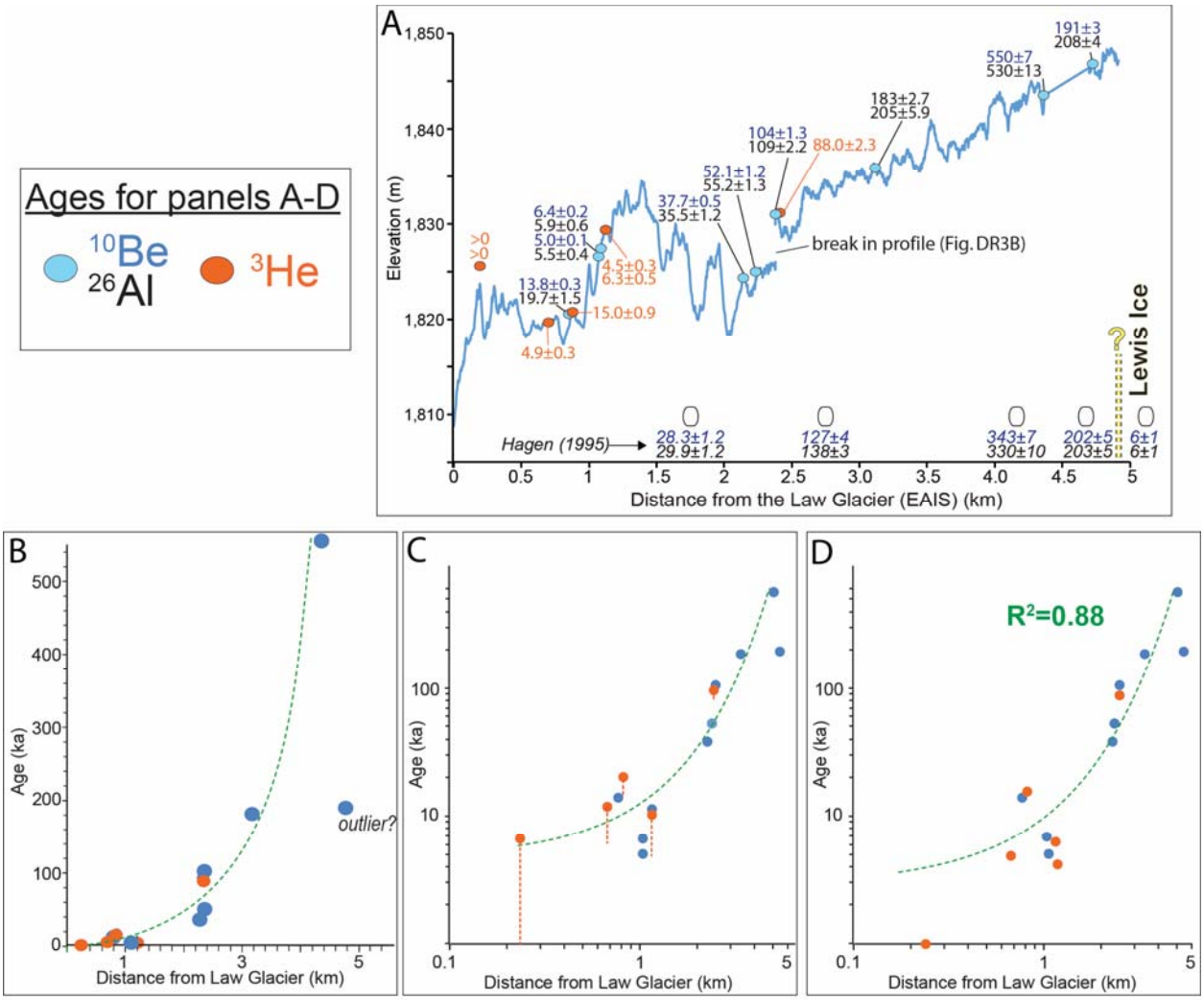

Figure DR4. Same as Figure 3, but following Figure DR3 above, it is assumed each ^{3}He measurement contains up to a maximum of 5.05 x 10^{6} atoms/g of noncosmogenic ^{3}He (nucleogenic or inherited, i.e., a maximum of 6.7 ka equivalent exposure ^{3}He age). This value is based on the two youngest samples, MAR-11-01 and 02 (Table DR4). This ^{3}He concentration is then subtracted from each sample's ^{3}He concentration (atoms/g), and then the ^{3}He ages are recalculated. As in Figure 2, it is assumed the ~190 ka ^{10}Be age from 5.6 km may be an outlier (see text).

Panels **(A) and (B).** Same as panels in Figure 3A and B in the main text but assuming each ^{3}He age has a maximum of ~6.7 ka equivalent of noncosmogenic He. The profile is from Bader et a. (2017). **(C)** For comparison, same as Figure DR4B panel just to the left, except plotted on log-log axes. Dashed vertical red lines represent subtraction of ~6.7 ka equivalent age from each sample. Note the change is less as the samples increase in age. Once at 100 ka the ^{3}He concentration in each sample is at least one order of magnitude higher than that in the 6.7 ka sample. **(D)** Same as Figure DR4C just to the left, except all ^{3}He ages are shown with the subtracted value. Dashed green line is exponential fit, which is shown merely to illustrate the progressive age increase with distance from the Law Glacier. For simplicity of illustration, only ^{10}Be and ^{3}He ages are shown in B to D; however, the ^{26}Al data indicate the same result given overall age concordance.

The key point of these four panels is to show the agreement of all 3 nuclides that the moraines steadily get older with distance from the relatively clean surface of the Law Glacier margin.

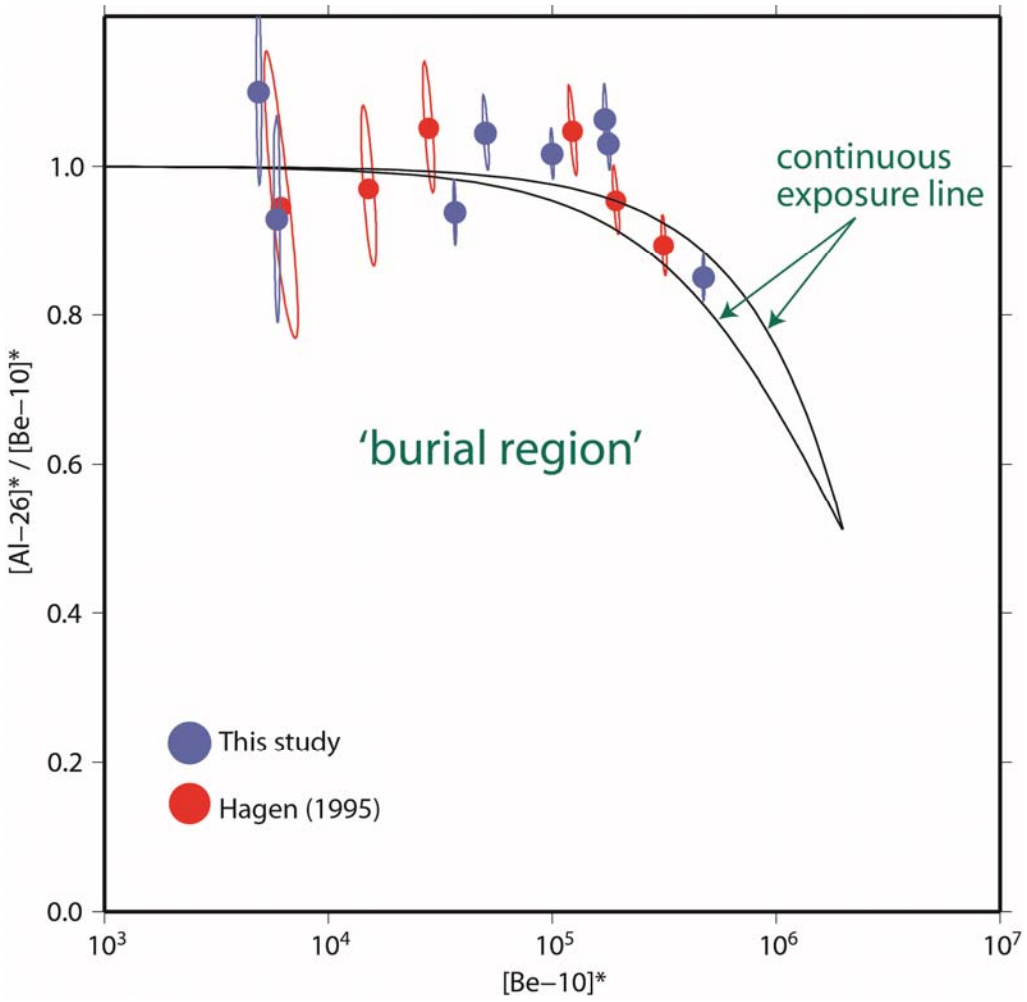

Figure DR5. A plot of $^{26}Al/^{10}Be$ versus ^{10}Be concentrations (atoms/g). The ratios are standardized (*) to 6.75, the Be-10 concentrations are relative to 07KNSTD and sea level high latitude (Balco et al., 2008). The plot indicates in a broad sense the samples do not indicate a complicated long-term history of exposure and burial (at least periods of burial greater than ~100,000 years). The data error envelops are 1σ analytical uncertainty.

Most ratios overlap with the continuous exposure line. 5 out of 15 ratios are slightly higher than the continuous exposure line, at 1σ (68% confidence level). However, 14 of 15 ratios overlap at 2σ (95% confidence level). The ratio of sample MAR-11-22 is not shown, as it lies above the plot. We are not sure of the reason 6 out of 15 samples, including MAR-11-22, provide slightly higher ratios (equivalent to >6.75 in Table DR1 below) at 1σ, than those represented along the continuous exposure line; especially, as most of the slightly-high ratio samples are in the first batch analyzed (Table DR1).

Table DR1. Surface-exposure sample details and ^{10}Be and ^{26}Al data.

Sample ID	Latitude (DD)	Longitude (DD)	Elevation (masl)[a]	Sample Thickness (cm)	Shielding correction	Quartz weight (g)	Carrier (Be) Added (g)	Total (Al) (g)
MAR-11-22	-84.18863	161.26488	1831	0.61	0.9993	3.0517	0.1858	1.9849
MAR-11-10	-84.22163	161.35674	1860	1.07	0.9997	10.0921	0.1860	1.0860
MAR-11-18	-84.19057	161.28288	1834	1.05	0.9988	15.1808	0.1864	1.9681
MAR-11-26	-84.2086	161.34976	1847	1.67	0.9997	10.0372	0.1863	1.7343
MAR-11-30	-84.1980	161.26189	1847	1.07	0.9967	8.5678	0.1871	1.4846
MAR-11-37	-84.2008	161.3199	1843	1.36	0.9994	10.1317	0.1838	1.8284
BLANK_1_2012May01							0.1861	1.0131
BLANK_2_2012May01							0.1836	--
MAR-11-14a	-84.21938	161.33736	1859	2.02	0.9997	4.0553	0.1825	1.6752
MAR-11-14b	-84.21938	161.33736	1859	2.02	0.9997	4.0632	0.1838	1.6917
MAR-11-17	-84.19072	161.2820	1835	1.10	0.9988	5.0766	0.1862	1.2010
MAR-11-33	-84.1970	161.25064	1866	1.87	0.9990	8.092	0.1854	1.5731
Blank_2_2013Jan24							0.1777	1.4472

Sample ID	^{10}Be/^{9}Be ± 1σ[b] 10^{-14}	[^{10}Be] ± 1σ (atoms x g^{-1}) 10^{5}	^{26}Al/^{27}Al ± 1σ[b] 10^{-14}	[^{26}Al] ±1σ (atoms x g^{-1}) 10^{5}	^{26}Al/^{10}Be ± 1σ
MAR-11-22	8.2612 ± 0.1843	3.3612 ± 0.0750	22.1414 ± 1.7538	32.1451 ± 2.5462	9.6 ± 0.8
MAR-11-10	363.7159 ± 5.2707	44.7971 ± 0.6492	1302.2702 ± 23.8240	312.7954 ± 5.7223	7.0 ± 0.2
MAR-11-18	14.6934 ± 0.2789	1.2057 ± 0.0229	31.0253 ± 2.3831	8.9783 ± 0.6896	7.4 ± 0.6
MAR-11-26	344.0529 ± 4.8424	42.6775 ± 0.6007	796.6776 ± 20.8441	307.2736 ± 8.0395	7.2 ± 0.2
MAR-11-30	85.7337 ± 2.0059	12.5134 ± 0.2928	229.0182 ± 5.3104	88.5792 ± 2.0539	7.1 ± 0.2
MAR-11-37	203.8014 ± 2.5791	24.7140 ± 0.3128	425.9514 ± 8.2534	171.5854 ± 3.3247	6.9 ± 0.2
BLANK_1_2012May01	0.0347 ± 0.0118	-- --	0.3601 ± 0.3601	-- --	5.7 ± 0.1
BLANK_2_2012May01	0.0314 ± 0.0105	-- --	-- --	-- --	5.8 ± 0.1
MAR-11-14a	390.8225 ± 4.2998	117.5487 ± 1.2933	725.8111 ± 13.5291	669.2379 ± 12.4746	6.3 ± 0.7
MAR-11-14b	387.3324 ± 4.2669	117.1206 ± 1.2902	734.4910 ± 13.7077	682.5808 ± 12.7389	6.3 ± 0.2
MAR-11-17	6.2607 ± 0.1874	1.5346 ± 0.0459	18.2125 ± 1.9192	9.6177 ± 1.0135	
MAR-11-33	59.0657 ± 0.7713	9.0480 ± 0.1181	131.9726 ± 4.4710	57.2676 ± 1.9401	
Blank_2_2013Jan24	0.2106 ± 0.0710	-- --	0.6938 ± 0.4907	-- --	

Note: Procedural blanks shown were processed identically to the samples, with one or two blanks accompanying each sample batch, respectively. ^{10}Be/Be and ^{26}Al/Al ratios measured relative to 07KNSTD (2.85^{-12}) and KNSTD standard (3.096^{-11}), respectively. Shown are analytical AMS uncertainties.

[a]Measured with a Trimble GPS system but undifferentiated cross checked with a handheld Garmin.

[b]MAR-11-14 was measured twice to test reproducibility.

Table DR2. ^{10}Be and ^{26}Al ages from Mt. Achernar.

Sample ID	^{10}Be Age ± 1σ (yrs)	^{26}Al Age ± 1σ (yrs)
MAR-11-22	13800 ± 310	19700 ± 1570
MAR-11-10	191100 ± 2910	207600 ± 4210
MAR-11-18	5000 ± 100	5500 ± 420
MAR-11-26	182500 ± 2690	204700 ± 5930
MAR-11-30	52100 ± 1240	55200 ± 1320
MAR-11-37	103700 ± 1350	109300 ± 2240
MAR-11-14a	552300 ± 7000	517400 ± 12600
MAR-11-14b	555200 ± 7000	536700 ± 13200
MAR-11-17	6360 ± 190	5890 ± 620
MAR-11-33	37700 ± 500	35500 ± 1220

Note: ^{10}Be and ^{26}Al ages calculated using the Southern Hemisphere production rate in Patagonia at ~50°S (Kaplan et al., 2011) and methods discussed in (Balco et al., 2008), including the constant production rate model ('St' scaling scheme) of Lal (1991)/Stone (2000). Although we use the rate in Kaplan et al. (2011) because it is at a higher latitude, it is statistically identical to the other Southern Hemisphere production rate, obtained in New Zealand (Putnam et al., 2010) If other scaling schemes are used (Balco et al., 2008), this has no effect on our conclusions. Age uncertainties include internal analytical error only. Uncertainties for production rate are ~3%. MAR-11-14 was measured twice to test reproducibility.

Table DR3. Surface-exposure sample details and ^{10}Be and ^{26}Al data recalculated from Hagen (1995).

Sample ID	Lat. (DD)	Long. (DD)	Elevation (m a.s.l.)	[^{10}Be] ± 1σ (atoms x g^{-1}) 10^5	[^{26}Al] ± 1σ (atoms x g^{-1}) 10^5	^{10}Be Age ± 1σ (yrs)	^{26}Al Age ± 1σ (yrs)	^{26}Al/^{10}Be ± 1σ
F-90-21	-81	161	1800	1.64 ± 0.19	9.49 ± 0.65	6170 ± 430	5840 ± 400	6.4 ± 0.9
F-90-18	-81	161	1800	51.22 ± 1.23	299.22 ± 6.58	202300 ± 5110	202500 ± 4900	6.5 ± 0.2
F-90-15	-81	161	1800	83.94 ± 1.56	459.4 ± 11.81	343200 ± 6960	330100 ± 10000	6.1 ± 0.2
F-90-14	-81	161	1800	4.03 ± 0.22	23.94 ± 1.29	15200 ± 830	14800 ± 800	6.6 ± 0.5
F-90-26	-81	161	1800	32.76 ± 1.02	209.88 ± 4.68	127000 ± 4080	137700 ± 3300	7.1 ± 0.3
F-90-27	-81	161	1800	7.47 ± 0.31	48.04 ± 1.82	28300 ± 1180	29900 ± 1200	7.1 ± 0.4

Note: We round off latitude and longitude because Hagen (1995) did not provide coordinates (prior to handheld GPS systems). To consider this uncertainty in position, for Figure 2 (and DR3), we draw a ~1 km circle round the approximate area indicated in Hagen (1995). We use a sample thickness of 1 cm and we do not correct for topographic shielding, given no values were provided. We assume shielding is similar to the data in Table DR1. These approximations have no effect on our findings and conclusions.

^{10}Be/Be and ^{26}Al/Al ratios measured relative to KNSTD standards (3.15^{-12} and 3.096^{-11}, respectively). Shown are analytical AMS uncertainties. $^{26/10}$Be ratios shown relative to 07KNSTD. Ages are calculated the same way as those in Table DR2.

Table DR4. Surface-exposure sample details and ^{3}He data.

Sample ID	Latitude (DD)	Longitude (DD)	Elevation (m a.s.l.)	Sample Thickness (cm)	Shielding correction	Pyroxene mass (g)	[^{3}He] ± 1σ (atoms x g^{-1}) 10^{5}	He^{3}/He^{4} ± 1σ 10^{-8}	He Age ± 1σ
MAR-11-08 (1)	-84.1910	161.2749	1829	1.07	0.999	0.0719	92.1456 ± 7.4858	8.6898 ± 1.1501	
MAR-11-08 (2)						0.0312	107.3186 ± 8.7819	11.3600 ± 0.9298	
					Average of the 2 analyses=		99.7321 ± 7.5865		12800 ± 970
MAR-11-23 (1)	-84.1870	161.2414	1825	1.35	0.999	0.0460	83.1669 ± 5.3854	10.8985 ± 0.8539	11400 ± 700
MAR-11-23 (2)						0.0371	93.9722 ± 6.8391	13.3016 ± 0.9684	
					Average of the 2 analyses=		88.5696 ± 5.4026		
MAR-11-52	-84.2286	161.2652	1830	1.09	0.999	0.0516	2380.1404 ± 55.2644	943.8149 ± 22.0226	304600 ± 7100
MAR-11-48 (1)	-84.2268	161.2755	1838	1.13	0.999	0.0254	823.7092 ± 22.4131	236.3370 ± 6.4346	104800 ± 2900
MAR-11-48 (2)						0.0263	828.0738 ± 22.7420	241.2585 ± 6.6291	105400 ± 2900
MAR-11-21 (1)	-84.1887	161.2672	1823	1.09	0.999	0.0285	176.8689 ± 9.4099	31.6898 ± 1.6862	22800 ± 1200
MAR-11-21 (2)						0.0333	155.7135 ± 8.1605	27.4441 ± 1.4385	20000 ± 1100
MAR-11-35	-84.2011	161.3220	1827	1.31	0.999	0.0315	735.4454 ± 19.5031	127.0875 ± 3.3719	94500 ± 2500
MAR-11-01	-84.1790	161.5365	1783	1.29	0.999	0.0290	50.2898 ± 4.4749	6.9904 ± 0.6221	6700 ± 590
MAR-11-02	-84.1791	161.5366	1785	0.57	0.999	0.0227	50.7600 ± 5.5215	10.4042 ± 1.1318	6700 ± 730
MAR-11-09	-84.1911	161.2725	1829	1.00	0.999	0.0262	85.2997 ± 5.9883	10.9323 ± 0.7676	10900 ± 770

Note: ^{3}He ages calculated using global production rate in Goehring et al. (2010), which incorporates the mid-high Southern Hemisphere rate obtained in Ackert et al. (2003). This rate was recently confirmed by Eaves et al. (2015). Ages are based on 'St,' (same as ^{10}Be-^{26}Al ages), the constant production rate scaling scheme (Lal, 1991/Stone 2000), although this has no effect on our conclusions. Age uncertainties include internal analytical error only.

MAR-11-08, MAR-11-23, MAR-11-48, and MAR-11-21 were each measured twice [(1) and (2)]: To test reproducibility between different preparers, MAR-11-48 and 21 were both processed twice, each time by a different person; the two respective analyses overlap at 1-2σ analytical uncertainty, and we show an average age on all Figures. For MAR-11-08 and 23, we averaged two machine measurements on the same sample, which also overlap at 1σ analytical uncertainty.

Last, for Figures DR3 and DR4 above, the average of the identical concentrations in MAR-11-01 and MAR-11-02 is used as a maximum possible value for noncosmogenic component of ^{3}He in. This amount potentially includes a magmatic component of ^{3}He, although studies have shown this to be insignificant for the Ferrar dolerite (Ackert and Kurz, 2004).

REFERENCES

Ackert Jr., R.P., and Kurz, M.D., 2004, Age and uplift rates of Sirius Group sediments in the Dominion Range Antarctica, from surface exposure dating and geomorphology, Global and Planetary Change, v. 42, p. 207-225.

Ackert, R.P., Singer, B.S., Guillou, H., Kaplan, M.R., and Kurz, M.D., 2003, Calibration of ^{3}He production rates against ^{40}Ar/^{39}Ar and K-Ar dated lava flows in Patagonia, Earth and Planetary Science Letters, v. 210, p. 119-136.

Bader, N.A., Licht, K.J., Kaplan, M.R., Kassab, C.,and Winckler, G., 2017, East Antarctic Ice Sheet stability since the mid-Pleistocene recorded in a high-elevation ice-cored moraine, accepted pending minor revisions, Quaternary Science Reviews, v.159, p. 88-102.

Balco, G., Stone, J.O, Lifton, N.A., and Dunai, T.J., 2008, A complete and easily accessible

means of calculating surface exposure ages or erosion rates from 10Be and 26Al measurements, Quaternary Geochronology, v. 3, p. 174-195.

Bintanja, R., 1999, On the glaciological, meteorological and climatological significance of Antarctic blue ice area, Reviews of Geophysics, v. 37, p. 337-359.

Bromley, G.R.M., Winckler, G., Schaefer, J.M., Kaplan, M.R., 2014, Pyroxene separation by HF leaching and its impact on helium isotopes, Quaternary Geochronology, v. 23, p. 1-8.

Campbell S., Balco G., Todd C., Conway H., Huybers K., Simmons C., Vermeulen M., 2013, Radar-detected englacial stratigraphy in the Pensacola Mountains, Antarctica: implications for recent changes in ice flow and accumulation, Annals of Glaciology, v. 54, p. 91-100.

Cassidy, W., Harvey, R., Schutt, J., Disle, G., Yanai, K. 1992, The meteorite collection sites of Antarctica. Meteroritics, v. 27, p. 490-525.

Chinn, T.J., 1991, Polar glacier margin and debris features, Memorie della Societa Geologica Italiana, v. 46, p. 25-44.

Chinn, T.J., 1994, Glacier disequilibrium in the Convoy Range, Transantarctic Mountains, Antarctica, Institute of Geological & Nuclear Sciences Contribution 217, p. 269-276.

Desilets, D., and Zreda, M., 2003, Spatial and temporal distribution of secondary cosmic-ray nucleon intensities and applications to in-situ cosmogenic dating, Earth and Planetary Science Letters, v. 206, p. 21-42.

Dunai,T.J., 2001, Influence of secular variation of the magnetic field on production rates of in situ produced cosmogenic nuclides, Earth and Planetary Science Letters, v. 193, p.197-212.

Eaves, S.R., Winckler, G., Schaefer, J.M., Vandergoes, M.J., Alloway, B.V., Mackintosh, A.N., Townsend, D.B., Ryan, M.T., and Li, X., 2015, A test of the cosmogenic ^{3}He production rate in the south-west Pacific (39°S), Journal of Quaternary Science, v. 30, p. 79-87.

Eaves, S.R., Mackintosh, A.N., Winckler, G., Schaefer, J.M., Alloway, B.V., Townsend, D.B., 2016, A Cosmogenic ^{3}He chronology of late Quaternary glacier fluctuations in North Island, New Zealand (39°S), Quaternary Science Reviews, v. 132, p. 40-56.

Faure, G., Mensing, T.M., 2010, The Transantarctic Mountains: Rocks, Ice, Metorites, and Water. Springer Science þ Business Media B.V. http://dx.doi.org/10.1007/978-90-481-9390-5_10, 289-469.

Fogwill, C.J., Hein, A.S., Bentley, M.J., and Sugden, D.E., 2011, Do blue-ice moraines in the Heritage Range show the West Antarctic ice sheet survived the last interglacial? Palaeogeography, Palaeoclimatology, Palaeoecology, v. 335-336, p. 61-70.

Goehring, B.M., Kurz, M.D., Balco, G., Schaefer, J.M., and Licciardi, J.M. and Lifton, N.A., 2010, A reevaluation of cosmogenic Helium-3 production rates, Quaternary Geochronology, v. 5, p. 410-18.

Hein, A., et al., 2016, Evidence for the stability of the West Antarctic Ice Sheet divide for 1.4 million years, Nature Communications, v. 7, p. 1-8.

Kaplan, M.R., Strelin, J.A., Schaefer, J.M., Denton, G.H., Finkel, R.C., Schwartz, R., Putnam, A.E., Vandergoes, M.J., Goehring, B.M., Travis, S.G., 2011, In-situ cosmogenic ^{10}Be production rate at Lago Argentino, Patagonia: Implications for late-glacial climate chronology, Earth and Planetary Science Letters, v. 309, p. 21–32.

Lal, D., 1991, Cosmic-ray labeling of erosion surfaces in-situ nuclide production rates and erosion models, Earth and Planetary Science Letters, v. 104, p. 424-439.

Lifton, N., Smart, D., and Shea, M., 2008, Scaling time-integrated in situ cosmogenic nuclide production rates using a continuous geomagnetic model, Earth and Planetary Science Letters, v. 268, p. 190-201.

Margerison, H.R., Phillips, W.M., Stuart, F.M., Sugden, D.E., 2005, Cosmogenic ^{3}He concentrations in ancient flood deposits from the Coombs Hills, northern Dry Valleys, East Antarctica: interpreting exposure ages and erosion rates, Earth Planetary Science Letters, v. 230, p. 163-175.

Nishiizumi, K., Imamura, M., Caffee, M.W., Southon, J.R., Finkel, R.C., and McAninch, J., 2007, Absolute calibration of ^{10}Be AMS standards: Nuclear Instruments and Methods in Physics Research B, v. 258, p. 403-413.

Pigati, J.S., and Lifton, N.A., 2004, Geomagnetic effects on time-integrated cosmogenic nuclide production with emphasis on in situ ^{14}C and ^{10}Be, Earth and Planetary Science Letters, v. 226, p. 193-205.

Putnam, A., Schaefer, J., Barrell, D.J.A., Vandergoes, M., Denton, G.H., Kaplan, M., Finkel, R.C., Schwartz, R., Goehring, B.M., Kelley, S., 2010, In situ cosmogenic ^{10}Be production-rate calibration from the Southern Alps, New Zealand, Journal of Quaternary Geochronology, v. 5, p. 392–409.

Scarrow, J.W., Balks, M.R., and Almond, P.C., 2014, Three soil chronosequences in recessional glacial deposits near the polar plateau, in the Central Transantarctic Mountains, Antarctica. Antarctic Science, doi:10.1017/S0954102014000078.

Schaefer, J.M., Denton, G.D., Kaplan, M. R., Putnam, A., Finkel , R.C., Barrell, D.J.A., Andersen, B.G., Schwartz, R. Mackintosh, A., Chinn, T., Schlüchter, C., 2009, High frequency glacier events in New Zealand during the Holocene are incoherent to the northern climate record, Science, v. 324, p. 622-625.

Sinisalo, A., and Moore, J.C., 2010, Antarctic blue ice areas – towards extracting paleoclimate information, Antarctic Science, v. 22, p. 99-115. Sinisalo, A, and Moore, J.C., 2010, Antarctic blue ice areas – towards extracting paleoclimate information, Antarctic Science, v. 22, p. 99-115.

Stone, J.O., 2000, Air pressure and cosmogenic isotope production: Journal Geophysical Research, v. 105, p. 23753-23759.

Whillans, I.M., and Cassidy, W.A., 1983, Catch a falling star: Meteorites and old ice, Science, v. 222, p. 55-57.